ROYAL SOCIETY
OF CHEMISTRY

PAPER

Check for updates

Cobalt-incorporated triclinic sodium aluminosilicate nanostructures: structural, optical, magnetic, and electrochemical investigations

Ali B. Abou Hammad,[a] A. M. Fathi,[b] A. A. Azab,[a] A. M. Mansour [ID] *[a] and Amany M. El Nahrawy [ID] [a]

Cobalt-doped sodium aluminosilicate nanostructures were synthesized *via* a sol–gel method and investigated for their structural, optical, magnetic, and electrochemical properties. X-ray diffraction confirmed the formation of a triclinic albite phase ($NaAlSi_3O_8$) with successful incorporation of Co^{2+} ions into the aluminosilicate framework. Optical absorption studies revealed new bands associated with tetrahedral Co^{2+} in Al_2O_3 nanocrystals, and a systematic decrease in the optical band gap with increasing Co content due to the creation of localized states in the band gap. Magnetic measurements demonstrated a transition from diamagnetic behavior in the undoped sample to ferromagnetic behavior in Co-doped samples, with enhanced saturation magnetization linked to exchange interactions. Electrochemical studies showed that the sample with the lowest Co content (ANSS1Co) exhibited the highest specific capacitance (187 F g^{-1} at 1 A g^{-1}) and excellent cycling stability, retaining 89.5% capacitance after 8000 cycles. These results highlight the potential of Co-doped sodium aluminosilicate nanostructures as stable electrode materials for energy storage applications.

1 Introduction

Alumino-silicate nanostructures, remarkable technological materials in scientific research, have garnered considerable interest due to their versatility in mechanical, magnetic, optical, and electrical properties.[1–3] These nanomaterials have gained significant prominence in both theoretical and experimental studies, owing to their distinct features at the nanoscale compared to their bulk counterparts and their potential applications across various fields. The combination of silica and aluminum oxides at the nanoscale exhibits unique characteristics, setting aluminosilicate apart for different applications.[4–6] The intricate interchange of silica and alumina inter-structure imparts enhanced thermal, structural, catalytic, and electrical properties to these nanostructures, assembling them as convenient candidates for advancements in diverse fields.

Aluminosilicate nanostructures can be synthesized through various methods, including sol–gel, hydrothermal, and template-assisted techniques.[7–10] The choice of synthesis method has a significant influence on the morphology, porosity, and surface properties of the resulting nanostructures.

The sol–gel method involves the hydrolysis and condensation of precursors, such as tetraethyl orthosilicate (TEOS) and aluminum alkoxides, in the presence of solvents and catalysts. This method allows for precise control over the composition, pore size, pore structure, and morphology of the resulting aluminosilicate nanostructures.[11–14]

Aluminosilicate nanostructures exhibit remarkable properties, such as high surface area, tunable pore size, thermal stability, and chemical resistance, making them suitable for a wide range of applications.[15,16] The unique combination of silica, sodium, and alumina at the nanoscale, along with their tunable morphology and surface properties, makes them suitable candidates for advancements in catalysis, energy storage, environmental remediation, and many other fields.[17,18] The unique pore structure and high thermal stability make aluminosilicate suitable for electrochemical and high-temperature catalytic processes, such as petrochemical processes, including fluid catalytic cracking (FCC) and hydrocracking of heavy oil fractions.[19–22]

Additionally, the porosity and surface area of these nanostructures can be optimized for adsorption and energy storage applications.[23] The porous structure and high surface area of aluminosilicate nanostructures make them excellent adsorbents for the removal of pollutants from water and air.[24] Their surface properties can be tailored by incorporating functional groups or modifying the chemical composition, enhancing their selectivity and affinity towards specific pollutants.

[a]*Solid State Physics Department, Physics Research Institute, National Research Centre (NRC), 33 El-Bohouth St., Dokki, Cairo, 12622, Egypt. E-mail: amamansour@gmail.com; ae.mansour@nrc.sci.eg*

[b]*Physical Chemistry Department, National Research Centre, 33 El-Bohouth, Dokki, Giza, 12622, Egypt*

Additionally, these nanostructures can be regenerated and reused, making them cost-effective and environmentally friendly.[25]

Aluminosilicate nanoparticles with crystal dimensions below 100 nm and considerable external surface areas provide more available active sites and short diffusion pathways.[25,26] Aluminosilicate nanostructures have shown great potential in energy storage applications, particularly in the development of high-performance lithium-ion batteries and supercapacitors.[27,28] In lithium-ion batteries, aluminosilicate nanostructures have been explored as anode materials, offering high capacity and improved cycling stability.[13] Their porous structure allows for the accommodation of volume changes during lithium insertion and extraction, mitigating the issue of electrode pulverization and enhancing the battery's cycle life. Furthermore, aluminosilicate nanostructures have been used as coating materials for cathodes, improving their electrochemical performance and thermal stability.[29,30] Their high surface area and electrical conductivity contribute to the high capacitance and energy density of these devices. Furthermore, their ability to accommodate various guest species within their pores allows for the design of novel energy storage systems, such as hybrid supercapacitors combining electrochemical double-layer capacitance and pseudocapacitance. The incorporation of transition metal ions or noble metal nanoparticles into the aluminosilicate framework can enhance their photocatalytic performance by promoting charge separation and increasing the generation of reactive oxygen species.[31,32] In addition, metal silicates such as (Mn, Co, Ni) silicates with a hollow sphere structure displayed high performance as electrode materials for supercapacitors, cobalt silicates gave high stability and theoretical capacity.[33] They are well-thought-out as potential materials for the electrodes of supercapacitors.[33,34]

Ongoing research efforts continue to explore novel synthesis strategies, property tuning, and innovative applications of these extraordinary nanostructures. Magnetic cobalt oxide nanocomposites have been used in magnetic resonance imaging (MRI), magnetic separation, magnetic drug delivery, and energy systems.[35,36] The development of scalable and cost-effective synthesis methods, as well as the integration of aluminosilicate nanostructures into practical devices and processes, will be crucial for realizing their full potential across various industries. The original nanosize of aluminosilicate and doped precursor nanoparticles as a clear solution during the sol gel process was fully conserved during crystallization. Such controlling synthesis endorses simultaneous reactions, including hydrolysis and/or condensation of silica, alumina, dopant species, formation and phase transfer of amorphous particles, nucleation, and crystal growth.[37,38]

In this work, the introduction of Co dopants into the sodium aluminosilicate structure nanocomposites aims to tailor their magnetic behavior for various applications. The magnetic properties of nanostructures play a decisive role in numerous technological fields, including data storage, magnetic sensors, spintronics, and nanomedicine. Cobalt, known for its magnetic properties, is introduced to enhance the magnetic behavior and storage of the nanocomposites. The superexchange interaction between Co^{2+} ions through the intermediate ions (O^{2-}) induces the magnetic coupling between Co^{2+} ions and affects the magnetic behavior, such as coercivity, exchange bias, and saturation magnetization. By employing this nanostructure, it is possible to tailor the magnetic properties to meet the demands of various applications, such as data storage,[39] magnetic sensors,[2,40] spintronic devices,[41,42] and nanomedicine for targeted drug delivery and imaging.[43,44] This nanostructure provides a comprehensive analysis of the magnetic properties of sodium aluminosilicate/silica cobalt nanocomposites, including saturation magnetization, coercivity, and the influence of cobalt on the magnetic properties.

In summary, this study aims to explore the effects of cobalt doping on the structural, optical, magnetic, and capacitive properties of sodium aluminosilicate nanostructures to tailor these properties for advanced technological applications. By investigating the behavior of these nanocomposites, we aim to provide new insights into the design and optimization of aluminosilicate-based materials for various applications, such as data storage, magnetic sensors, energy storage, and optoelectronics. Our findings could pave the way for the development of novel materials with enhanced performance and functionality.

2 Experimental work

2.1. Synthesis of Al_2O_3:Na_2O:SiO_2@SiO_2:Co nanocomposites

The sol–gel solution for TEOS was prepared using a TEOS : H_2O : HCl molar ratio of 1.3 : 11 : 0.02. This ratio was selected to provide: (i) excess water to drive complete hydrolysis of TEOS, (ii) a small catalytic amount of HCl to accelerate hydrolysis/condensation, and (iii) a slight TEOS excess to ensure the required silica content in the final oxide.

The ethanol/HCl mixture was used to produce systems with good resistance to calcination and a high surface area.[3,45–47]

Al_2O_3:Na_2O:SiO_2 sols were obtained by homogenization of the solution of $Si(OC_2H_5)_4$ in ethanol with the solution of Al_2O_3 and Na_2O in ethanol/H_2O, with a precise addition of HCl as a catalyst for the process. First, TEOS was dissolved in ethanol and stirred vigorously. Deionized water and HCl were then added dropwise under continuous stirring at room temperature to initiate hydrolysis as represented in eqn (1). The acid-catalyzed hydrolysis step converts TEOS to silanols, while condensation yields the silica network:

$$Si(OC_2H_5)_4 + 2H_2O \rightarrow SiO_2 + 4C_2H_5OH \qquad (1)$$
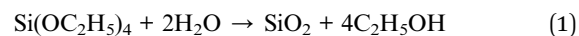
After mixing the TEOS solution with the Al_2O_3 and Na_2O solutions under stirring for 1 hour at 40 °C, the resulting sols were dried at 100 °C.

For the Co-doped system, 0.8 mg of the dried Al_2O_3:Na_2O:SiO_2 powder was dispersed into a mixture consisting of 7 mL TEOS, cobalt acetate ($x = 1–5$ mol%), 10 mL distilled water, 5 mL TEOS, 10 mL ethanol, and HCl under stirring. This produced a homogeneous sol in which different concentrations of cobalt (1–5 mol%) were introduced. The sols were kept under stirring and subsequently dried at 100 °C to form gels.

Subsequently, different concentrations (1–5 mol%) of Co NPs, are synthesized by the same steps. The obtained undoped Al_2O_3:Na_2O:SiO_2 (ANS) and Co-doped ANSS(1–5)Co samples were finally calcined at 700 °C, yielding the desired oxide nanostructures. The preparation steps are summarized schematically in Fig. 1.

2.2. Characterization

XRD record of the Al_2O_3:Na_2O:SiO_2@SiO_2:Co nanocrystalline was collected at ambient conditions and filtered using Cu Kα radiation; tube operated at 30 mA and 45 kV, with Ni filter to eliminate Kβ on Empyrean diffractometer by Panalytical (Almelo; The Netherlands) in (2θ) 20–80°. Morphological properties were determined by using a Transmission Electron Microscope (TEM 2010, JEOL at 200 kV, Japan). FTIR studies were carried out with a JASCO 460 PLUS, FTIR spectrometer, with a range from 400 to 2000 cm^{-1}. Diffuse reflectance was measured in the wavelength range of 200–2500 nm through a double-beam spectrophotometer (JASCO: V-570 model).

2.3. Electrochemical measurements

Electrochemical performance was evaluated using a three-electrode system with the prepared nanostructures as the working electrode. The active material (Al_2O_3:Na_2O:SiO_2:Co) was coated onto nickel foam/current collector, with a mass loading of 4.3, 5.4, 7.7, and 8.8 mg for ANS, ANSS1Co, ANSS2Co, ANSS3Co, and ANSS5Co, respectively. This mass was used for the calculation of specific capacitance and related electrochemical parameters. To investigate the electrochemical performances, the prepared materials were used as a working electrode in a three-electrode cell that contained 1.0 M KOH solution as an electrolyte. The other two electrodes were pure Pt-wire as a counter electrode and (Ag/AgCl) ($E° = 0.203$ V versus SHE) as a reference electrode. To prepare the material of the working electrode, the specific weight of the prepared material was mixed with PVDF (polyvinylidene fluoride) and carbon black by a certain ratio (80 : 10 : 10), and DMF (N,N-dimethyl formamide) was used to make a suspension. Ultra-sonication for 30 min was applied to the mixture to form a slurry, then 20 μl of the slurry was dropped by micropipette onto the surface of nickel foam. Then, it dried at 60 °C for 4 h, then at room temperature overnight. Before using the Ni foam, it was degreased in acetone and etched for 15 min in 1 M HCl, and subsequently washed in water and ethanol for 5 min each. The cyclic voltammetry and charge–discharge were carried out at room temperature by using Origalys OGS 200 potentiostat/galvanostat. The samples were measured at different scan
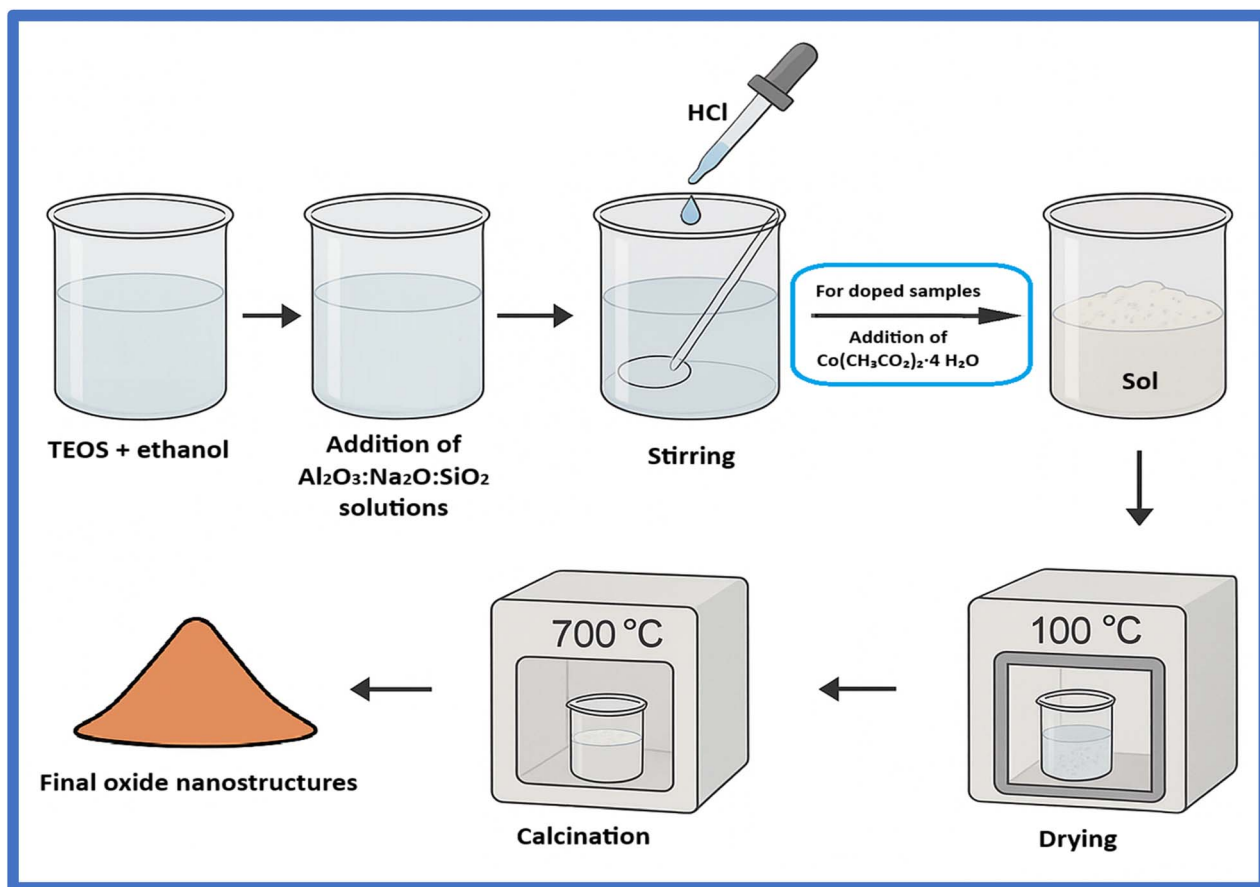

Fig. 1 Schematic illustration of the sol–gel synthesis and calcination process for preparing cobalt-doped sodium aluminosilicate nanocomposites.

rates from 0.01–0.3 V s^{-1}, covering a potential window (−0.6 to 0.8 V) (*versus* Ag/AgCl).

3 Results and discussion

3.1. Phase purity (XRD)

Fig. 2 displays the XRD pattern of the sodium aluminosilicate fabricated and calcinated at 700 °C. X-ray diffraction is primarily utilized to identify the crystal structure of the finely ground, fabricated sample powders. Fig. 2 shows that the fabricated samples are well-crystallized and do not exhibit any hump, indicating the absence of short-range order (amorphous structure). The samples calcined at 700 °C showed significant peaks for albite structure at 2θ (°) = 21.7°, 23.5°, 28.27°, 30.22°, 31,23°, 35.9°, 48.4°, and 56.9°. The observed peaks are assigned to the triclinic structure of NaAlSi$_3$O$_8$ (JCPDS 96-900-0530), known as albite.[48] The XRD chart doesn't show other peaks besides those of the albite structure (NaAlSi$_3$O$_8$), confirming that the sol–gel method is suitable for fabricating high-purity sodium aluminosilicate with a higher crystalline structure in the albite phase.

The XRD of cobalt-doped sodium aluminosilicate samples shows a uniform structure similar to the structure of sodium aluminosilicate. They are crystallized in the triclinic phase, which is matched with the same XRD card as the pure sample. The XRD patterns of all samples are consistent; therefore, this indicates that the introduction of Co^{2+} doesn't alter the crystal structure of the prepared samples. This behavior confirms that Co^{2+} is completely dissolved in the structure of the host albite phase NaAlSi$_3$O$_8$ and mostly substitutes the Al^{3+} ions within the aluminosilicate framework. The only difference is observed in the 2° range (21° to 30°), where some peaks become more pronounced, which can be attributed to the Co^{2+} enhanced crystal structure of the prepared samples. This structural assignment is further supported by FTIR spectra (Section 3.2), where Si–O–Al linkages were detected, consistent with the aluminosilicate lattice of albite. The coexistence of minor SiO$_2$ and Al$_2$O$_3$ reflections suggests partial retention of unreacted oxides, but the predominant crystalline phase remains albite.

Table 1 The XRD data of the samples, 2θ (°), d-spacing (Å), FWHM (°), and crystallite size (nm)

| Sample	2θ (°)	d-Spacing (Å)	FWHM (°)	Crystallite size (nm)
S11	21.8482	4.06809	0.1791	34
S12	21.7689	4.07935	0.090	37
S13	21.7785	4.08095	0.1791	38

The crystallite size of the prepared sodium aluminosilicate is estimated by the Scherrer equation from the most intense peak (20−1). The Scherrer equation is given by:

$$G = \frac{0.9\lambda}{\beta \cos(\theta)} \quad (2)$$

G is the average crystallite size, λ is the wavelength of the X-rays, and β is the full width at half maximum (FWHM) of the diffraction peak. The estimated crystallite size of the samples is listed in Table 1.

3.2. FTIR results

The functional features of sodium aluminosilicate@Co–SiO$_2$ NPs were examined over FTIR in the range from 400–4000 cm^{-1} (Fig. 3). The FTIR-spectroscopy of the aluminum sodium silicate (ANSS) doped with (1–5 mol%) Co nanocomposites, provided valuable insights into its molecular structure and bonding characteristics. The broad absorption bands around 3500 cm^{-1} are attributed to the (O–H) stretching modes of the hydroxyl groups, representative of the existence of adsorbed water molecules on the surface of the nanocomposite.[49–52] The strong absorption bands observed around 1093 cm^{-1} are ascribed to the asymmetric stretching vibrations of the Si–O–Si bonds, and their intensity increased with the Co ratio, characteristic of the silicate structure.[3,45,47,53] The band appearing at 795 cm^{-1} corresponds to the bending vibrations of Na–O–Si, Al–O–Si, and Na–O–Al links, and their intensity increases with the Co ratio,
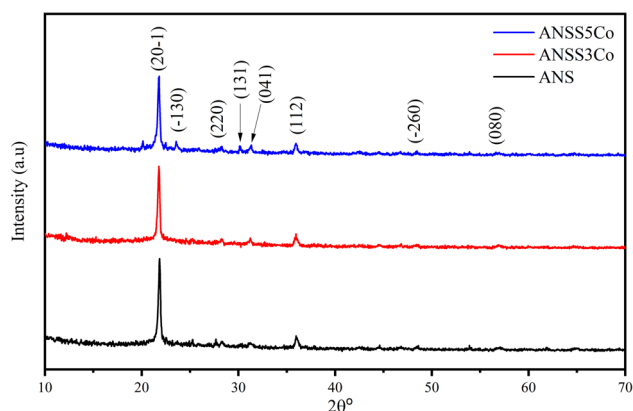
Fig. 2 The XRD pattern of ANS doped with (1–5 mol%) Co^{2+} nanoparticles.
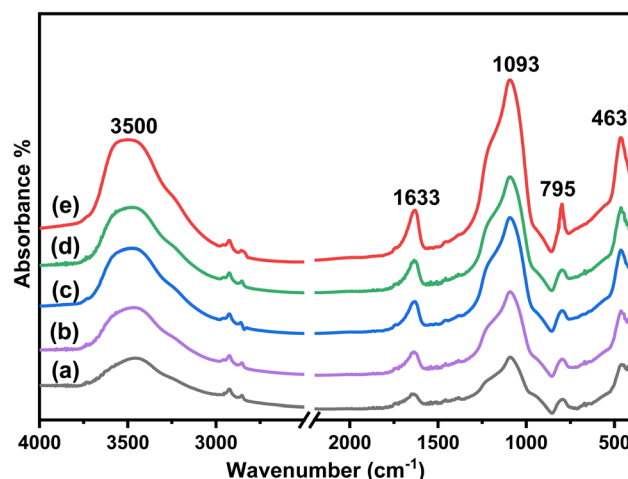
Fig. 3 FTIR spectra of (a) ANS doped with (b) 1, (c) 2, (d) 3, and (e) 5 mol% Co NPs.

revealing the integration of aluminum into the silicate structure.[54,55]

The presence of Na–O–Si, Al–O–Si, and Si–O stretching vibrations is branded by the absorption band at 463 cm^{-1}, confirming the presence of Na, Al, and Co in the nanocomposite.[26,47,54] The increase in the band's intensity around 400–1100 cm^{-1} confirms the successful incorporation of Co NPs into the ANS nanocomposite structure. The grape-like ANS structure highlights the bonding interactions within the silicate nanocomposite.

3.3. TEM

The TEM images (Fig. 4) illustrate the nanostructural features of sodium aluminosilicate doped with 3 and 5 mol% CoO/SiO$_2$. TEM images enable the visualization of individual sodium alumino-silicate and doped with Co nanoparticles, providing insights into their nanosize, nanospherical shape, and internal structure. The TEM images (Fig. 4a–c) revealed a distinctive grape-like morphology of the Co-doped sodium aluminosilicate nanostructures. The images showed well-dispersed nanoparticles with uniform size and shape, forming clusters reminiscent of grape bunches. Also, TEM illustrates that numerous clustering nanospherical nanoparticles are present, supporting the well formation of complex silicate-based nanoparticles. TEM (Fig. 4a–c) can identify the distinct features of nanoporous, agglomeration, and jointed with others in the fabricated samples.

Particle sizes were determined from TEM images using statistical analysis of multiple particles, and the results are presented as histograms (Fig. 4d). The average particle sizes obtained were ∼30 nm (ANS), ∼33 nm (ANSS3Co), and ∼37 nm (ANSS5Co), which are consistent with the crystallite sizes calculated from XRD (34–38 nm). Although a single particle can be labeled for illustration, we note that the reported values are based on statistical distribution for higher accuracy. Herein, the crystallite diameter calculated from XRD closely matches the particle diameter observed in TEM, indicating consistency between the two measurement techniques (XRD and TEM). This match indicates that the nanoparticles are likely single crystallites instead of agglomerates of smaller crystallites. This is crucial for considering the structural properties and supporting its quality for various applications.

3.4. Optical discussions

The fundamental techniques for determining the band structure of materials primarily involve optical measurements. These measurements enable the comprehensive exploration of a material's electrical and atomic properties by analyzing its optical characteristics. Critical parameters such as the absorption edge, optical energy band, and optical transitions of solid materials can be assessed through absorption studies. These optical transitions may be characterized as either direct or indirect and may exhibit a nature that is either direct or forbidden.

The diffuse reflectance (R_d) spectra of the prepared samples at room temperature are illustrated in Fig. 5. Within the
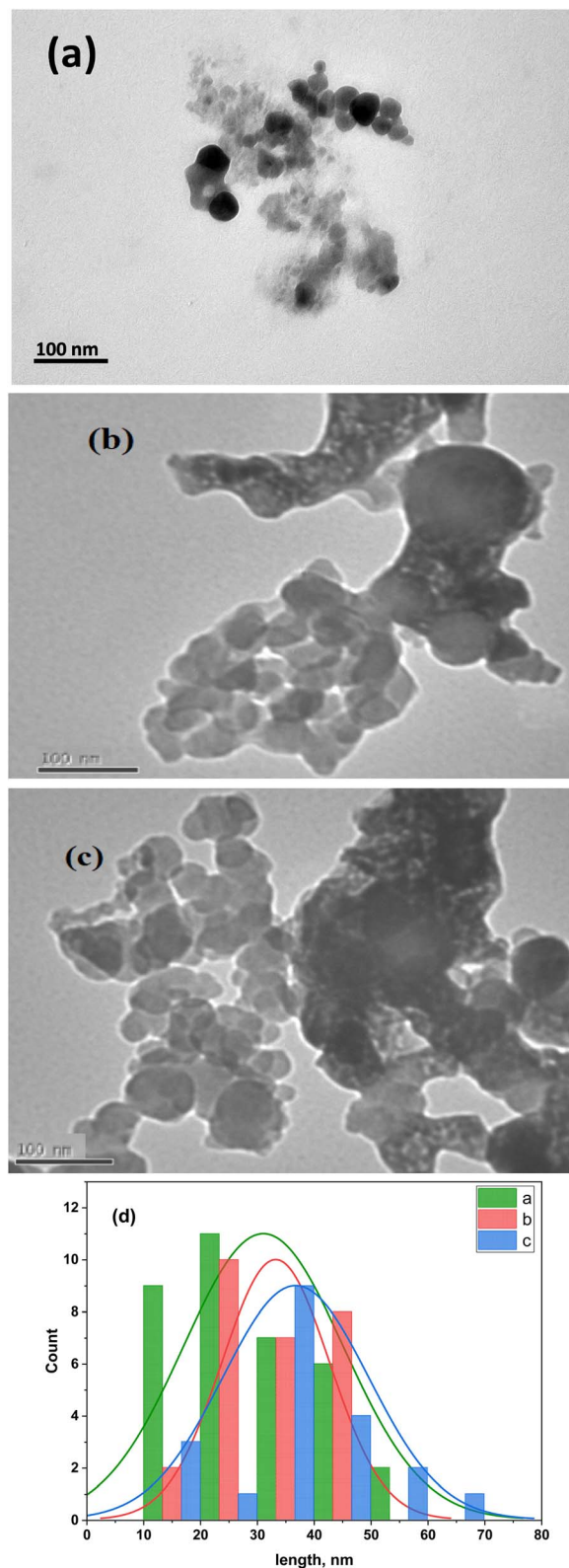

Fig. 4 TEM images of (a) undoped ANS, (b) ANSS3Co, and (c) ANSS5Co nanostructures showing grape-like morphology. (d) Particle size distribution histograms derived from TEM analysis of multiple particles.
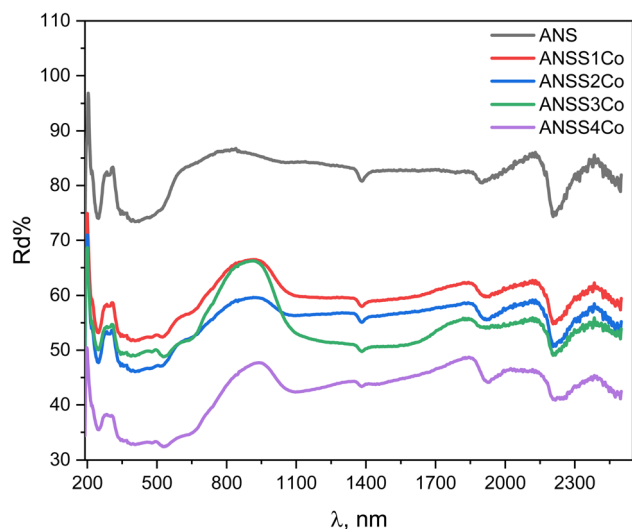
Fig. 5 Room temperature diffuse reflectance spectra of the ANS coated with SiO_2–Co nanocomposites.

wavelength range of 200 nm to 2500 nm, a subtle alteration is noted in the diffuse reflectance for all samples. By the addition of Co, the Rd decreases. Notably, interference peaks are discerned at higher wavelengths.[27]

Fig. 6 presents the absorbance spectra of the prepared samples. The $Al_2O_3Na_2OSiO_2$ sample demonstrates minimal absorbance. The absorbance increases by increasing the SiO_2–Co coating ratio. The $Al_2O_3Na_2OSiO_2$ sample exhibits absorption bands at 248, 430, 1379, and 2209 nm. The absorption at 248 has resulted from the charge carrier's excitation and transition from the valence band to the conduction band.[55] The peak at 430 nm may be due to the complexation process, where oxygen vacancies increase in the composite structure.[56] The very weak peak at 1379 nm was also observed, which means that the silanol group (Si–OH) was difficult to break in the system.[56]
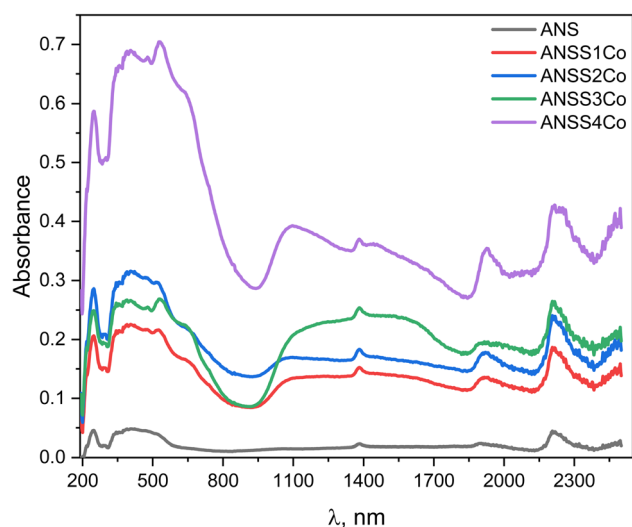

Fig. 6 Absorbance the ANS coated with SiO_2–Co nanocomposites.

Finally, the absorption at 2209 nm is due to the presence of oxygen vacancies or any defects present in these ceramics.[57]

The new absorption bands observed upon incorporation of Co into the SiO_2–Al_2O_3 framework can be interpreted as described by Xiulan Duan et al.[56] These absorption bands are characteristic of tetrahedral Co^{2+} ions in Al_2O_3 nanocrystals, confirming that Co^{2+} is integrated into the host structure rather than forming a separate surface coating. Co^{2+} ion has a d^7 electronic configuration. The crystal field splitting of the energy levels of Co^{2+} in a tetrahedral crystal field is similar to that of a d^3 electronic configuration in an octahedral field, except for the value of the crystal field parameter D_q, which is smaller in the tetrahedral case. The tetrahedral crystal field splits the ground ^4F state into $^4A_2$, $^4T_2$, and $^4T_1$ levels, of which the $^4A_2$ lies lowest. The absorption feature demonstrated that the Al_2O_3 nanocrystals were formed (also confirmed by the XRD pattern). Si^{4+} ion existing in the aluminosilicate glass-ceramics served as a tetravalent compensating ion. With the increase of Co^{2+} ions entering into the tetrahedral sites of Al_2O_3 crystals, the intensity of the absorption bands increased. This enhancement is attributed to the effect of cobalt incorporation, which introduces localized electronic states and induces local structural distortions in the SiO_2–Al_2O_3 framework.[58] These changes strengthen the optical transitions of Co^{2+} ions, rather than being related to variations in silicate concentration (which remained constant during synthesis).[57]

One can derive estimates for the band gap and its values through the application of the Kubelka–Munk relation:[59,60]

$$F(R_\infty) = C(h\nu - E_g)^n/h\nu \tag{3}$$

The Kubelka–Munk formula, denoted as $F(R)$, incorporates photon energy ($h\nu$), optical band gap (E_g), and the nature of electronic transition (n at 1/2 for direct and 2 for indirect).[26]

In Fig. 7(a) and (b) $(\alpha h\nu)^{1/2}$ and $(\alpha h\nu)^2$ are plotted against ($h\nu$) to determine the type and value of the gap transition. Observations indicate the presence of two energy transitions (for both direct and indirect cases) for every concentration. These are identified as the first and second π–π^* excitations, with the first designated as the optical transition bandgap.[60,61] Notably, the values of both the 1st and 2nd excitation transitions decrease with the increasing Co content, as illustrated in Fig. 7(c). Both direct and indirect energy gap transitions are possible, with indirect transitions having a higher value, as shown in Fig. 7(c). Consequently, a direct transition is more probable.[62–64] The decrease in energy transitions in composite samples is due to CoO creating localized energy states in the band gap, aiding the movement of charge carriers from the valence to the conduction band.[65,66]

3.5. Magnetic properties

Fig. 8 shows the magnetic hysteresis loop for nanostructures of sodium aluminosilicate doped with (1–5 mol%) cobalt (ANSS/(1–5)Co) nanostructures in an external applied magnetic field ±20 kG, carried out at room temperature. The inset in Fig. 8 shows M–H loops for the pure sample and $x = 4$. The pure sample demonstrates diamagnetic properties while the core–
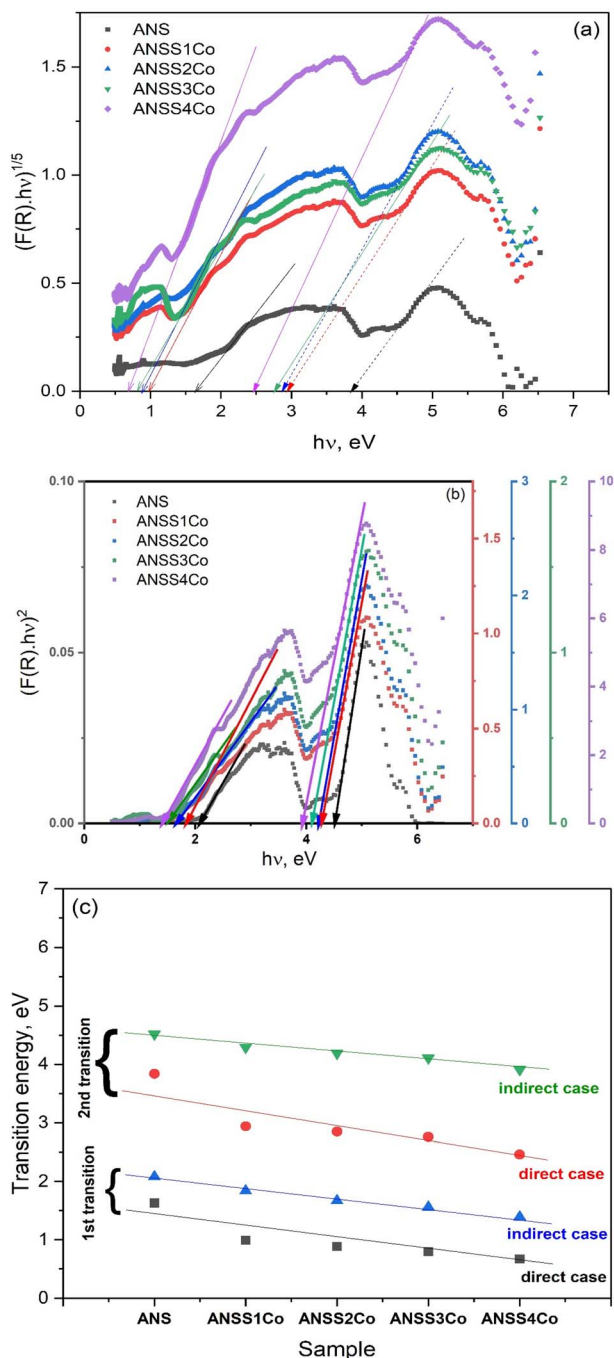
Fig. 7 Plot of (a) $(\alpha h\nu)^{1/2}$ and (b) $(\alpha h\nu)^2$ against ($h\nu$), (c) the behavior of transition energies with the addition of Co.

shell ANSS/xCo nanocomposites show ferromagnetic characteristics. The magnetic parameters, such as saturation magnetization (M_s), remnant magnetization (M_r), coercivity, squareness, and magnetic exchange, are tabulated in Table 1. The results in Table 1 show that the M_s increases with increasing Co content, with a huge increase in magnetization from that of ANS/1Co to that of ANS/2Co (4 times), M_s of ANS/3Co is equal to 2.5 times that of ANS/2Co, M_s of ANS/4Co is more than 8 times ANS/3Co. This huge increase in

magnetization is due to the exchange interaction between the core and shell of the nanocomposite.[67,68] This interaction leads to changes in the magnetization behavior of the core and can affect its overall magnetic properties.[69,70] Furthermore, super-exchange interactions can induce magnetic coupling between Co^{2+} ions. This exchange interaction induces the magnetization of the albite nanocomposite and affects the overall magnetic properties.[71] The overall magnetism can be either enhanced or suppressed, depending on the strength and nature of the coupling. The magnetization alignment and distribution within the nanocomposite can be influenced by these interactions.[72] The squareness ratio, M_r/M_s, is equal 0.08 for ANS/1Co and increases to 0.27 for ANS/3Co and then decreases to 0.21 for ANS/4Co. These results show that increasing the Co content enhances the squareness ratio.

The results in Table 2 show that the magnetic coercivity increases with increasing Co content from 453 G at $x = 1$ to reach 543 G at $x = 3$ and then decreases to 536 G at $x = 4$. The coercivity of albite can be modified by manipulating the composition. By controlling the composition and structure, it is feasible to customize their coercivity to suit certain applications, such as permanent magnets, magnetic recording media, and magnetic sensors.[73–76] The (M–H) hysteresis loops were found to shift in the horizontal direction along the magnetic field axis. The phenomenon of the magnetization hysteresis loop shifting is called the exchange bias effect.[69,72] The exchange bias was attributed to the magnetic exchange coupling between the ferromagnetic (FM), antiferromagnetic (AFM), para-magnetic, and diamagnetic surfaces.[77] The exchange bias in magnetic nanoparticles is caused by surface effects, which introduce additional anisotropy and result in a stable magne-tization.[78] The ANSSxCo nanocomposites showed exchange bias H_{EB} as obtained in Table 2. From the reported values of exchange bias, all nanocomposites demonstrate a positive value of exchange bias with values 10.1, 101.2, 42.5, and 2.5 G for ANSS1Co, ANSS2Co, ANSS3Co, and ANSS3Co, respectively. The sample ANSS2Co showed the maximum value (101.2 G) and then ANS/3Co (42.5 G). The observed enhancement in magne-tization can be attributed to core–shell exchange interactions, where the ferromagnetic Co-rich core is exchange-coupled with the surrounding aluminosilicate/SiO$_2$ shell. This coupling stabilizes spin alignment at the interface and suppresses spin canting, resulting in enhanced saturation magnetization. A schematic illustration of this mechanism is presented in Fig. 9, showing how the core–shell architecture promotes exchange coupling and contributes to high-performance properties relevant to data storage, biomedical imaging, and magnetic sensing.

3.6. Electrochemical measurements

To show the qualities of prepared materials as an electrode for capacitors, cyclic voltammetry (CV), and galvanostatic charge–discharge (GCD) were performed in 1.0 M KOH. The CV curves of Fig. 10 show that the best potential range for the electro-chemical performance of these materials was −0.6–0.8 V. To identify the advantage of doping with Co on the electrochemical
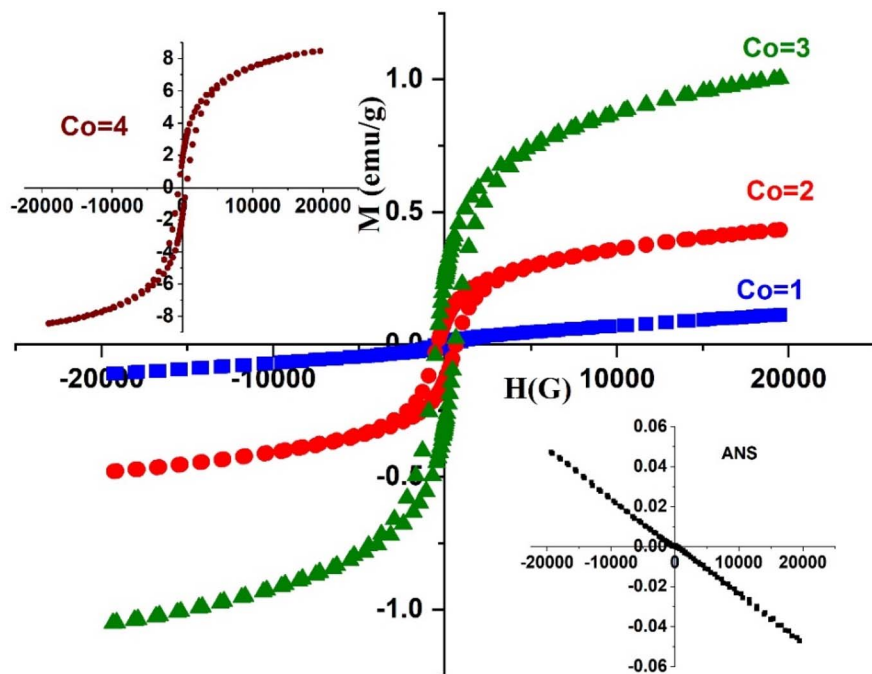
Fig. 8 *M, M−H* loops for pure ANS and ANSSxCo nanocomposites.

Table 2 The magnetic parameters extracted from the magnetic hysteresis loops of the field sweeping within ±20 kOe at room temperature

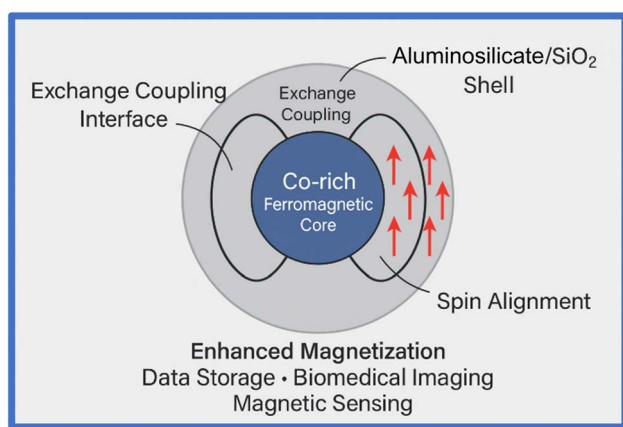|	M_s (emu g^{-1})	M_r (emu g^{-1})	H_c (G)	Sq	H_E
ANSS1Co	0.111	0.009	453.4	0.08	10.1
ANSS2CO	0.456	0.111	540.1	0.24	101.2
ANSS3Co	1.027	0.275	543.8	0.27	42.5
ANSS4Co	8.4	1.74	536	0.21	2.5

Fig. 9 Schematic representation of core–shell exchange interactions. Ferromagnetic Co-rich cores are surrounded by an aluminosilicate/SiO₂ shell.

behavior of ANS, CV curves for nickel foam (NF), the undoped ANS, and the doped ANS with different Co concentration (ANSS1Co, ANSS2Co, ANSS3Co, and ANSS5Co) at scan rate 0.1 V

s^{-1} were investigated in Fig. 10(a), where the area under the curve increases by doping with Co NPs indicating large specific capacitance, this increase is due to the decrease in energy transitions in ANS with doping of CoO which facilitate the charge transfer as mentioned in the optical discussion section.[79] The CV shape shows a pair of redox peaks in the potential range from 0.1 to 0.7 V, which indicates pseudo-capacitance behavior and a battery-like performance. The redox peaks that appear in the CV curves are due to the transfer of the hydroxyl ions from the solution to be adsorbed on the Si–O on the ANS surface, resulting in the release of electrons from the surface. After doping with Co, the probability of OH shut-tling increases; therefore, the capacity increases, as shown in the following equation:[80]
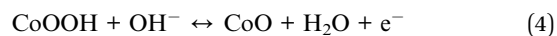
$$CoOOH + OH^- \leftrightarrow CoO + H_2O + e^- \tag{4}$$

Fig. 10(b)–(f) depict the CV curves of ANS, ANSS1Co, ANSS2Co, ANSS3Co, and ANSS5Co at various scan rates from 0.01 V s^{-1} to 0.3 V s^{-1}. There is a shift in the peak potential with increasing the scan rate, indicating a quasi-reversible charac-teristic of the peak. In addition to an upsurge in the peak current upon rising the scan rate was observed, which indicated high capacitive behavior.

To investigate the kinetics of the storage process, the relation between i_p and v was determined according to the following equation:[81]

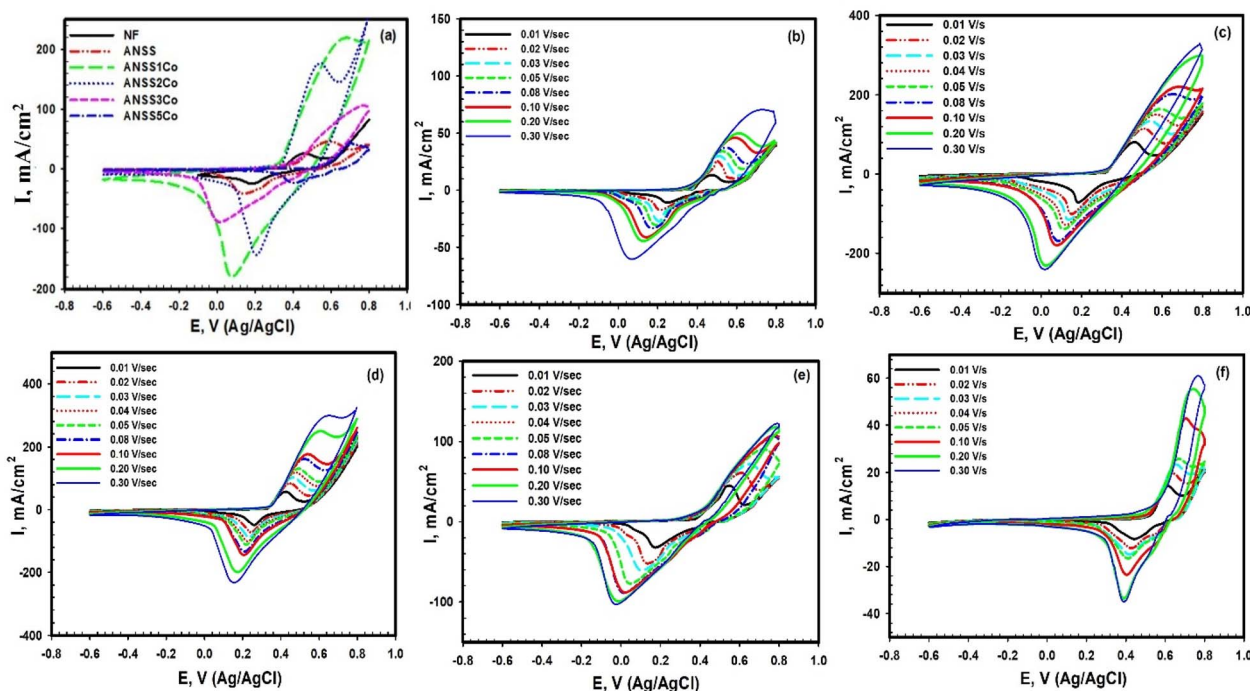$$\log i_p = \log a + b \log v \tag{5}$$

Fig. 10 Cyclic voltammetry for (a) NF, ANS, ANSS1Co, ANSS2Co, ANSS3Co, and ANSS4Co in 1.0 M KOH aqueous solution at scan rate 0.1 V s^{-1}, (b) ANS, (c) ANSS1Co, (d) ANSS2Co, (e) ANSS3Co, (f) ANSS4Co at different scan rates (0.01–0.3 V s^{-1}).

The slope of this linear relation is b, as observed from Fig. 11(a), the value of b tends to be 0.5, suggesting that the charging reaction is controlled by the diffusion of the ions to the electrode surface.[82,83] The specific capacitance C_s of the samples can be calculated by using the area under the voltammogram ($\int I dV$) according to the following formula:

$$C_s = \frac{\int I dV}{2mv\Delta V} \tag{6}$$

where m is the active mass of the sample, ΔV is the potential window, and v is the scan rate. The specific capacitance and the

scan rate relationship are shown in Fig. 11(b). The relation shows a decrease in the specific capacitance with increasing the scan rate. As the number of active sites decreases at high scan rates because of the ions' insufficient time to interact with the electrode material, which lowers the specific capacitance.[84,85] As noticeable from Fig. 11(b), ANSS1Co shows the largest specific capacitance value, and the specific capacitance decreases with doping but is still higher than the undoped one, except ANSS5Co, which indicates the crucial of the amount of Co on the electrochemical behavior. A greater rise in the amount of doped Co can increase the particle size as mentioned in the
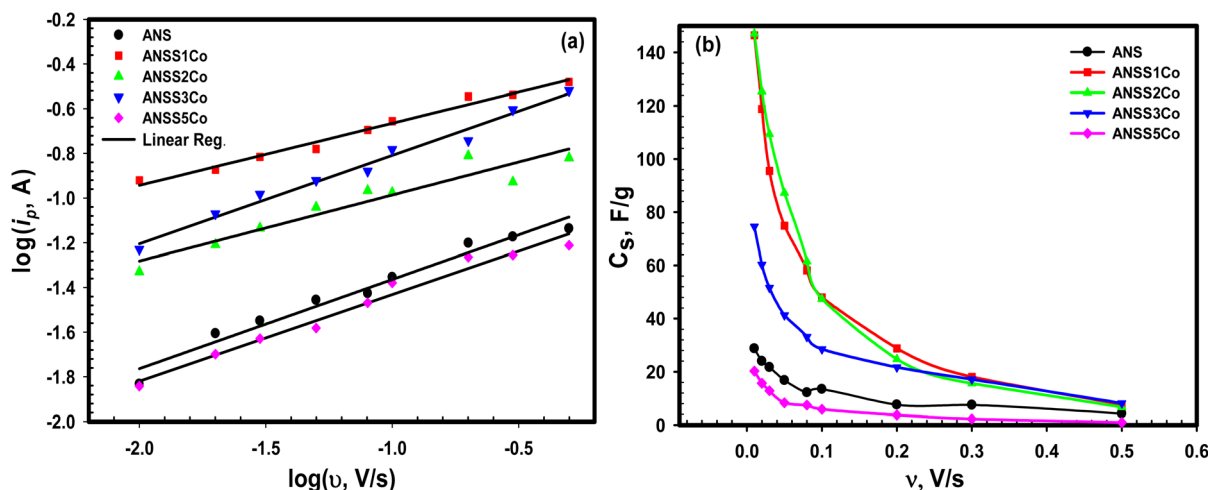

Fig. 11 (a) The relation between log v and log current of the peak (i_p), (b) specific capacitance as a function of the scan rate for the samples.

XRD and TEM characterization, which influences the nanostructure integrity, that leads to a decrease in the specific capacitance.[86]

A greater rise in the amount of doped Co can increase the particle size as mentioned in the XRD and TEM characterization, which influences the nanostructure integrity, leading to a decrease in the specific capacitance, where a small particle size can increase the energy density and the kinetic properties of the materials.[86,87]

Fig. 12(a) represents the discharging curves for ANS, ANSS1Co, ANSS2Co, ANSS3Co, and ANSS5Co at 1.0 A g^{-1}, where the discharge curves show a steady plateau that deviates from the linear behavior, which confirms the pseudocapacitive behavior.[88,89] The time of discharge increases by doping with Co; however, ANS/1Co represents the longest time, indicating that it is the most capacitive material. More doping of Co leads to a decrease in the discharge time, which represents similar results to the CV results.

The effect of the applied current on the charge–discharge behaviour was studied for the five samples as shown in Fig. 12(b)–(f), and the curves showed a decrease in the discharge time with rising applied current. The following equation was used to calculate the specific capacitances (C_s) at different current densities:[90,91]

$$C_s = \frac{I \int V(t)dt}{m(\Delta V)^2} \qquad (7)$$

where $\int V(t)dt$ is the integration of the area under the discharge curve, ΔV is the potential window (−0.3 to 0.5 V), I give the current (A), and m is the active mass of the material (g).

The calculated specific capacitance was inversely related to the applied current densities as shown in Fig. 13(a), where at high current, there is not enough time for the diffusion of the ions from the solution to spread on the electrode active area.[92] The highest specific capacitance value approaching 187.6 F g^{-1} was for ANSS1Co which contains the lowest content of Co.

The stability of cycling for the ANSS1Co electrode was performed by repeating the charge–discharge test at 10 A g^{-1} for 8000 cycles, and the relation between the capacitance retention and the coulombic efficiency with the number of cycles for ANSS1Co was plotted as shown in Fig. 13(b), the first ten cycles are illustrated in the inset Fig. 13(b). The specific capacitance of the first cycle at 10 A g^{-1} was 11.6 F g^{-1} decayed to 9.6 F g^{-1} after 10 cycles maintaining 83.4% of its initial value, then increased to 12.51 F g^{-1} through the 1200 cycles and decreased again to reach a constant value of 10.3 F g^{-1} after 8000 cycles maintaining 89.48% of its initial value, and the coulombic efficiency of nearly 100% was observed. This behavior suggests good long-term charge–discharge cycling stability for ANSS1Co. The decrease in the specific capacitance through the first 10 cycles may be due to the degradation of part of the materials to the solution; however, the increase in the solution temperature during the long-term cycling results in an increase in the specific capacitance.[93,94]

To investigate any structural change for the material through cycling, the electrode after cycling was analyzed by XRD, FTIR, SEM, and EDX.

The X-ray diffraction pattern of the cycled sample (Fig. 14) is dominated by the characteristic reflections of face-centred cubic nickel attributable to the Ni foam substrate, with the
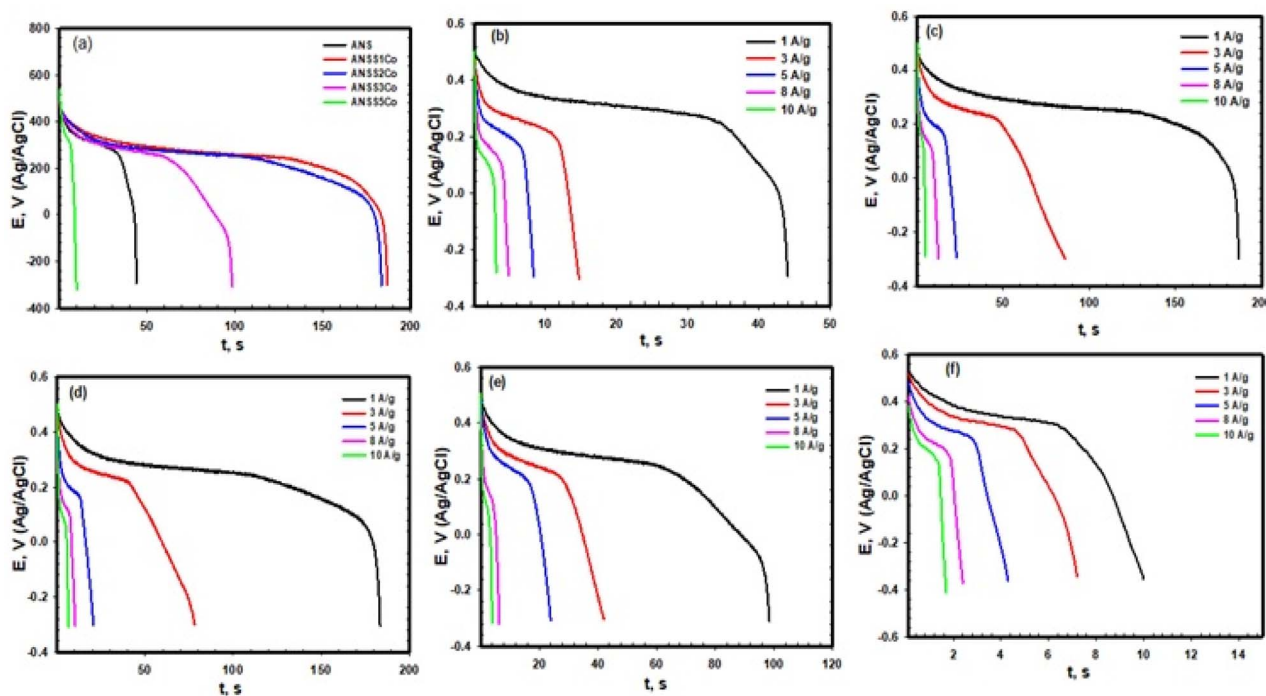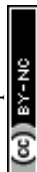

Fig. 12 Galvanostatic charge–discharge curves for (a) all samples at 1.0 A g^{-1}, and at various current densities and in 1.0 M KOH for (b) ANS, (c) ANSS1Co, (d) ANSS2Co (e) ANSS3Co (f) ANSS5Co.
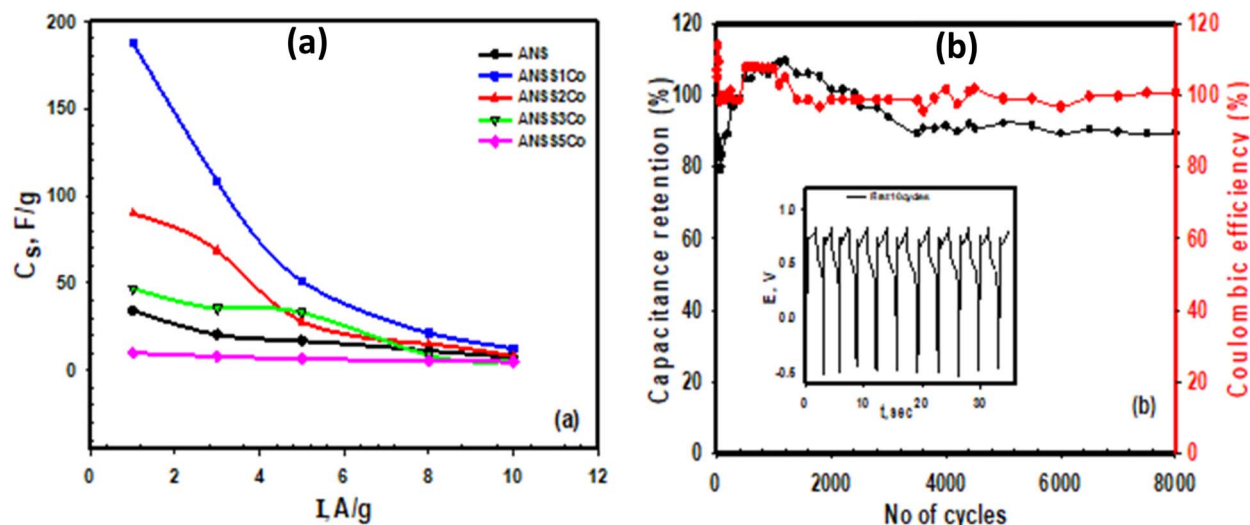
Fig. 13 (a) The relation between the specific capacitance as a function of the applied current density for all the samples, and (b) capacitance retention and the coulombic efficiency of ANSS1Co as a function of the charge–discharge cycling number (current density: 10 A g^{-1}). The inset figure shows the charge/discharge curves for the first 10 cycles.
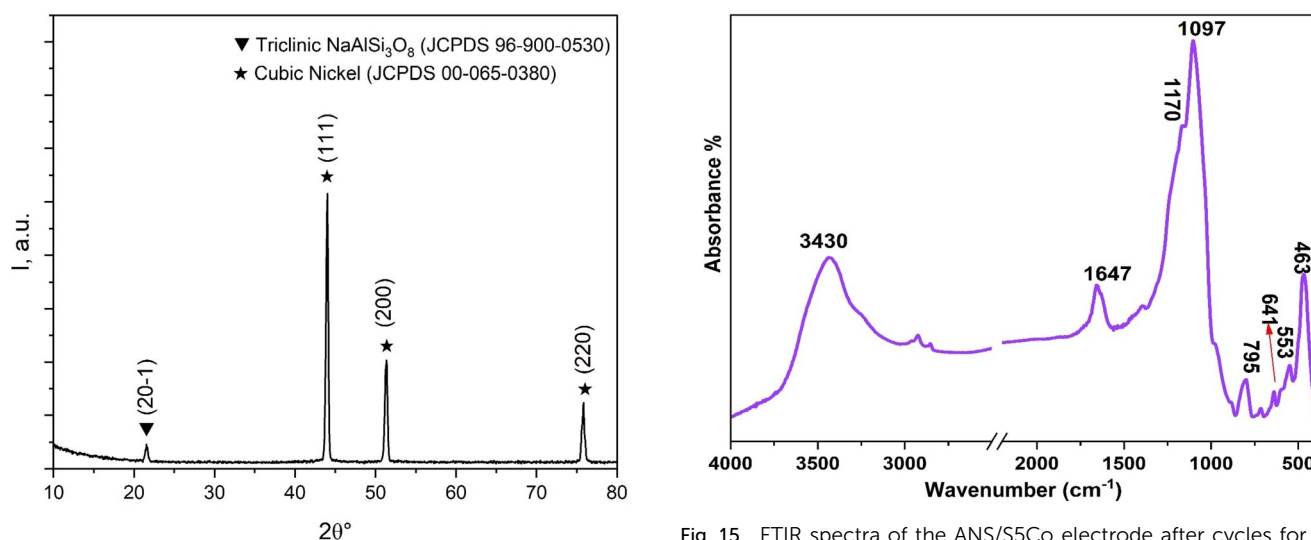

Fig. 14 X-ray diffraction (XRD) pattern of Ni foam loaded with cobalt-doped sodium aluminosilicate after electrochemical cycling.

Fig. 15 FTIR spectra of the ANS/S5Co electrode after cycles for the sample 3 mol% Co NPs.

three strong peaks at $\approx 43.9°$, $\approx 51.3°$ and $\approx 75.8°$ assigned to the (111), (200) and (220) lattice planes of fcc Ni, respectively; these intense nickel lines account for the vast majority of diffracted intensity and therefore mask weaker contributions from low-loading or poorly crystalline surface phases.[95]

A much weaker diffraction feature is observed at low angle ($\sim 21.8°$), which corresponds to a triclinic $NaAlSi_3O_8$ (albite/alkali feldspar type) phase in accordance with JCPDS 96-900-0530. The low intensity of this peak relative to the nickel reflections indicates a small mass fraction and/or a low crystallinity of the sodium aluminosilicate after cycling.

The FTIR in Fig. 15 shows the characteristic silicate fingerprints (asymmetric Si–O–Si stretch near ~ 1093 cm^{-1}, and the

bending band near ~ 795 cm^{-1}, 670 cm^{-1}, and 463 cm^{-1}) remain in the spectrum of the electrode after cycling, showing that the bulk aluminosilicate framework is largely preserved after electrochemical cycling.[96,97]

The increase in the O–H stretching band (~ 3430 cm^{-1}) after cycling indicates water adsorption, hydroxyl species formation from KOH, and/or Co–OH surface formation, reflecting electrode hydroxylation during long-term cycling in alkaline electrolyte. Also, the electrode after cycles shows slight changes in the lower-wavenumber region (400–900 cm^{-1}). These changes are related to various vibrations (surface oxidation/hydroxylation of cobalt/sodium aluminosilicate species) resulting from exposure to KOH and the redox processes during charge/discharge. This indicates surface chemical modification
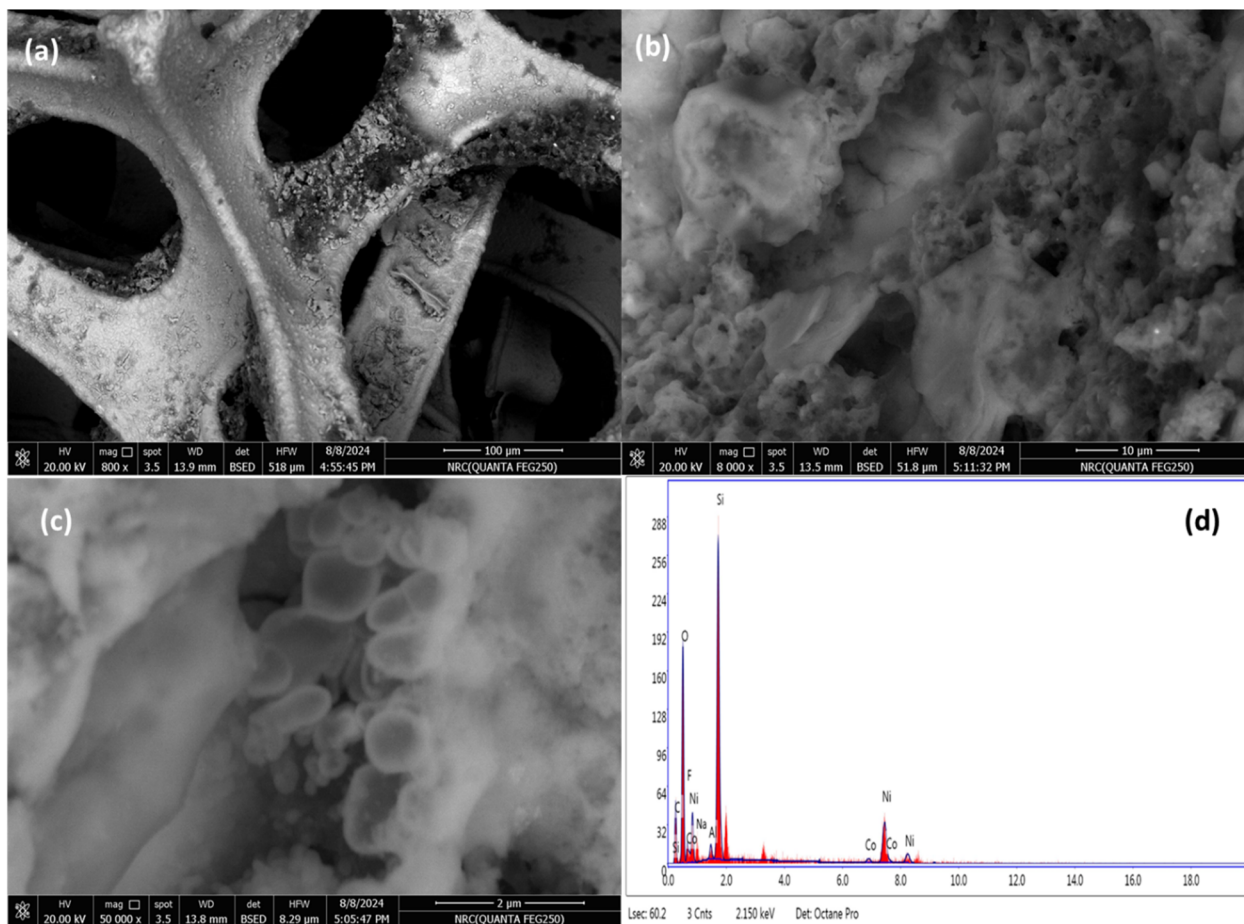
Fig. 16 SEM for Ni foam loaded with ANSS1Co after cycling at magnification: (a) 100×, (b) 8000×, (c) 50 000×, and (d) EDX for the same area.

Table 3 Comparative analysis of Co-based silicates for their use in a supercapacitor[a]

Sample ID	C_s (F g^{-1})	ΔE (V)	Cycle retention	Electrolyte	Ref.
CoSiO$_4$ (CoSi)	193, 1.0 A g^{-1}	−0.1 to 0.55	—	3 M KOH	17
PCoSi	256, 1.0 A g^{-1}		84%, 10 000 cycles		
CoSi	214, 1.0 A g^{-1}	0–0.5	83%, 10 000 cycles	6 M KOH	18
(Ni,Co)$_3$Si$_2$O$_5$(OH)$_4$	144, 1.0 A g^{-1}	0–0.5	99%, 10 000 cycles	1 M NaOH	19
CoSi@MnO$_2$	490, 1.0 A g^{-1}	−0.5 to 0.6	45%, 5000 cycles	3 M KOH	20
e-CoSi	267, 1.0 A g^{-1}	0–0.5	90%, 10 000 cycles	6 M KOH	21
Co$_3$(Si$_2$O$_5$)$_2$(OH)$_2$	237, 5.7 A g^{-1}	0.1–0.55	95%, 150 cycles	6 M KOH	22
CoSi/GO	511, 0.5 A g^{-1}	−0.1 to 0.55	84%, 10 000 cycles	3 M KOH	23
ANSS1Co	187.6, 1.0 A g^{-1}	−0.3 to 0.5	89.4%, 8000 cycles	1 M KOH	This work

[a] GO: graphene oxide, P: phosphorus-doped, e-CoSi: etched cobalt silicate.

of the Co-containing sites. Overall, the comparison of FTIR before and after cycling demonstrates that while the bulk framework remains intact, surface chemistry is modified during cycling, consistent with the observed electrochemical behavior. The change appears in the FTIR spectrum at 400–1200 cm^{-1} after cycling, the vibration of the Si–O–Ni bonds.[96,98] These surface changes are consistent with (and help explain) the electrode's electrochemical behavior and the SEM/EDX observation that the coating remains adherent but is hydroxylated/modified after long cycling in KOH.

The morphology of the electrode after cycling was investigated by using scanning electron microscopy (Fig. 16). The film of the material coated on the nickel foam skeleton and the pores are kept open (Fig. 16(a)–(c)), allowing the diffusion of ions.[99,100] Furthermore, the coat is still adherent to the foam after long-term cycling in KOH. The high-magnification SEM image shows spherical crystals that reveal a grape-like structure, as mentioned also in the TEM results. The materials on the nickel foam were also confirmed by using an energy-dispersive X-ray spectrometer (EDX) as shown in Fig. 16(d), which indicates

Paper
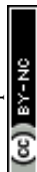
the presence of elements Ni, Co, Al, Na, Si, F, and O on the nickel foam surface, confirming the presence of sodium aluminosilicate incorporated with Co.

The observed high cycling stability (89.5% retention after 8000 cycles) together with SEM/EDX characterization demonstrates the robustness of the electrode material.

The comparison of the current results with the published data in the literature is illustrated in Table 3. It was found that the studied materials are consistent with the published and, in some cases, better than those previously obtained for Co-based silicate compounds, despite the difference in morphology, crystallography, and the doping or combination of other materials.

4 Conclusions

Sodium aluminosilicate nanostructure has been successfully formed by the sol–gel method and sintered at 700 °C. Detailed spectroscopic characterizations (XRD, FTIR, optical) clearly confirmed that there exist excellent interactions between ANS/SCo in the formed nanocomposites. The high-resolution TEM images provided a clear visualization of the crystallographic planes, indicating high crystallinity of the synthesized ANS/SCo. Analyzing absorption reveals key parameters, including the absorption edge, optical energy band, and transitions. The incorporation of Co into the SiO_2–Al_2O_3 nanostructure induces additional absorption bands connected to tetrahedral Co^{2+} ions in Al_2O_3 nanocrystals. The nanocomposites exhibit significant changes in magnetic properties with increasing Co ratio, transitioning from diamagnetic to ferromagnetic behavior. A higher Co ratio enhances M_s and impacts exchange interactions, including dipolar interactions and exchange coupling, which affect the nanocomposite magnetization. The exchange bias effect observed in these ANSSxCo materials is promising for applications in spintronics, nanomedicine, and data storage. The calculated specific capacitance values from both the cyclic voltammetry and charge–discharge techniques showed higher values of the coated samples with SiO_2–Co, however, ANSS1Co represented the highest one due to the increase in the particle size of the samples with increasing Co content. In addition, good long-term charge–discharge cycling stability for ANSS1Co was maintained at high current density, which suggested the practical application of the prepared materials as electrodes for energy storage capacitors. This work focused on intrinsic material properties using a three-electrode system. Future studies will extend to two-electrode device configurations to further assess practical application potential.

Ethical statement

This research doesn't involve human participants and/or animals.

Author contributions

All authors conceived and designed the experiments; analyzed and interpreted the data; contributed reagents, materials, analysis tools, or data; and wrote the paper.

Conflicts of interest

The authors declare no competing interests.

Data availability

All data generated or analyzed during this study are included in this published article.

Acknowledgements

References

1 A. M. El Nahrawy, B. A. Hemdan, A. B. Abou Hammad, A. L. K. Abia and A. M. Bakr, Microstructure and Antimicrobial Properties of Bioactive Cobalt Co-Doped Copper Aluminosilicate Nanocrystallines, *Silicon*, 2020, **12**, 2317–2327.

2 A. M. Elnahrawy, Y. S. Kim and A. I. Ali, Synthesis of hybrid chitosan/calcium aluminosilicate using a sol-gel method for optical applications, *J. Alloys Compd.*, 2016, **676**, 432–439.

3 J. H. Jin, H. Um, J. H. Oh, Y. Huh, Y. Jung and D. Kim, Gadolinium silicate-coated porous silicon nanoparticles as an MRI contrast agent and drug delivery carrier, *Mater. Chem. Phys.*, 2022, **287**, 126345.

4 A. M. Elnahrawy, Y. S. Kim and A. I. Ali, Synthesis of hybrid chitosan/calcium aluminosilicate using a sol-gel method for optical applications, *J. Alloys Compd.*, 2016, **676**, 432–439.

5 A. B. Abou Hammad, A. M. Elnahrawy, A. M. Youssef and A. M. Youssef, Sol gel synthesis of hybrid chitosan/calcium aluminosilicate nanocomposite membranes and its application as support for CO2 sensor, *Int. J. Biol. Macromol.*, 2019, **125**, 503–509.

6 O. Saber, A. Alshehab, N. M. Shaalan, A. M. Hegazy, F. K. Aljasem and A. Osama, Fabrication of a Novel Silica–Alumina-Based Photocatalyst Incorporating Carbon Nanotubes and Nanofiber Nanostructures Using an Unconventional Technique for Light-Driven Water Purification, *Catalysts*, 2025, **15**, 452.

7 S. Xue, Y. Bi, S. Ackah, Z. Li, B. Li, B. Wang, Y. Wang, Y. Li and D. Prusky, Sodium silicate treatment accelerates biosynthesis and polymerization of suberin polyaliphatics monomers at wounds of muskmelon, *Food Chem.*, 2023, **417**, 135847.

8 A. M. E. Nahrawy, A. A. Moez and A. M. Saad, Sol-Gel Preparation and Spectroscopic Properties of Modified

Sodium Silicate/Tartrazine Dye Nanocomposite, *Silicon*, 2018, **10**, 2117–2122.

9 H. Zhu, K. Liu, Z. Meng, H. Wang and Y. Li, Properties and Preparation of Alumina Nanomaterials and Their Application in Catalysis, *Micro*, 2025, **5**, 38.

10 S. Jovita, A. T. Melenia, E. Santoso, R. Subagyo, R. Tamim, N. Asikin-Mijan, H. Holilah, H. Bahruji, R. E. Nugraha, A. A. Jalil, H. Tehubijuluw, M. Ulfa and D. Prasetyoko, Mesoporous aluminosilicate from nanocellulose template: effect of porosity, morphology and catalytic activity for biofuel production, *Renew. Energy*, 2025, **250**, 123293.

11 M. M. Azim and A. Stark, Ionothermal synthesis and characterisation of Mn-, Co-, Fe- and Ni-containing aluminophosphates, *Microporous Mesoporous Mater.*, 2018, **272**, 251–259.

12 A. M. E. Nahrawy, A. M. Mansour, A. M. Bakr and A. B. A. Hammad, Terahertz and UV–VIS Spectroscopy Evaluation of Copper Doped Zinc Magnesium Titanate Nanoceramics Prepared via Sol-Gel Method, *ECS J. Solid State Sci. Technol.*, 2021, **10**, 063007.

13 A. H. Lu and F. Schüth, Nanocasting: A Versatile Strategy for Creating Nanostructured Porous Materials, *Adv. Mater.*, 2006, **18**, 1793–1805.

14 Y. Wan and D. Zhao, On the Controllable Soft-Templating Approach to Mesoporous Silicates, *Chem. Rev.*, 2007, **107**, 2821–2860.

15 J. C. Védrine, Acid-base characterization of heterogeneous catalysts: an up-to-date overview, *Res. Chem. Intermed.*, 2015, **41**, 9387–9423.

16 A. M. El Nahrawy, B. A. Hemdan, A. M. Mansour, A. Elzwawy and A. B. Abou Hammad, Integrated use of nickel cobalt aluminoferrite/Ni2+ nano-crystallites supported with SiO2 for optomagnetic and biomedical applications, *Mater. Sci. Eng., B*, 2021, **274**, 115491.

17 D. Zhang, C. Liu, Y. Yang, X. Tang, Z. Jiang, L. Su, X. Li, Z. Chen and W. Yang, Systematic investigation on preparation and characterization of silica shell microencapsulated phase change materials based on sodium silicate precursor, *Colloids Surf., A*, 2023, **667**, 131328.

18 S. S. Owoeye, S. M. Abegunde and B. Oji, Effects of process variable on synthesis and characterization of amorphous silica nanoparticles using sodium silicate solutions as precursor by sol–gel method, *Nano-Struct. Nano-Objects*, 2021, **25**, 100625.

19 D. Zhao, W. Huang, M. N. Rahaman, D. E. Day and D. Wang, Mechanism for converting Al2O3-containing borate glass to hydroxyapatite in aqueous phosphate solution, *Acta Biomater.*, 2009, **5**(4), 1265.

20 R. H. French, Electronic Band Structure of Al2O3, with Comparison to Alon and AlN, *J. Am. Ceram. Soc.*, 1990, **73**, 477–489.

21 Y. Liu, W. Zhang and T. J. Pinnavaia, Steam-Stable MSU-S Aluminosilicate Mesostructures Assembled from Zeolite ZSM-5 and Zeolite Beta Seeds, *Angew. Chem., Int. Ed.*, 2001, **113**(7), 1295.

22 A. B. A. Hammad, A. M. El Nahrawy, D. M. Atia, H. T. El-Madany and A. M. Mansour, Effect of Cu co-doping on the microstructure and optical properties of alumino-zinc thin films for optoelectronic applications, *Int. J. Mater. Eng. Innovat.*, 2021, **12**, 18–36.

23 X. Xu, Y. Dong, Q. Hu, N. Si and C. Zhang, Electrochemical Hydrogen Storage Materials: State-of-the-Art and Future Perspectives, *Energy Fuels*, 2024, **38**, 7579–7613.

24 H. S. Jo, H. Kim and S. Y. Yoon, Synthesis and Characterization of Mesoporous Aluminum Silicate and Its Adsorption for Pb (II) Ions and Methylene Blue in Aqueous Solution, *Materials*, 2022, **15**(10), 3562.

25 A.-H. Lu, D. Zhao and Y. Wan, *Nanocasting: A Versatile Strategy for Creating Nanostructured Porous Materials*, 2009.

26 A. M. El Nahrawy, A. Elzwawy, A. B. Abou Hammad and A. M. Mansour, Influence of NiO on structural, optical, and magnetic properties of Al2O3–P2O5–Na2O magnetic porous nanocomposites nucleated by SiO2, *Solid State Sci.*, 2020, **108**, 106454.

27 M. F. Al-Hilli and K. T. Al-Rasoul, Characterization of alumino-silicate glass/kaolinite composite, *Ceram. Int.*, 2013, **39**, 5855–5862.

28 Y. Tao, H. Kanoh, L. Abrams and K. Kaneko, Mesopore-Modified Zeolites: Preparation, Characterization, and Applications, *Chem. Rev.*, 2006, **106**, 896–910.

29 A. R. Jayakrishnan, J. P. B. Silva, K. Kamakshi, D. Dastan, V. Annapureddy, M. Pereira and K. C. Sekhar, Are lead-free relaxor ferroelectric materials the most promising candidates for energy storage capacitors?, *Prog. Mater. Sci.*, 2023, **132**, 101046.

30 Y. Liu and T. J. Pinnavaia, Aluminosilicate Nanoparticles for Catalytic Hydrocarbon Cracking, *J. Am. Chem. Soc.*, 2003, **125**, 2376–2377.

31 S. O. Tan, O. Çiçek, Ç. G. Türk and Ş. Altındal, Dielectric properties, electric modulus and conductivity profiles of Al/Al2O3/p-Si type MOS capacitor in large frequency and bias interval, *Eng. Sci. Technol.*, 2022, **27**, 101017.

32 S. Supiyani, H. Agusnar, P. Sugita and I. Nainggolan, Preparation sodium silicate from rice husk to synthesize silica nanoparticles by sol-gel method for adsorption water in analysis of methamphetamine, *S. Afr. J. Chem. Eng.*, 2022, **40**, 80.

33 X. Li, S. Ding, X. Xiao, J. Shao, J. Wei, H. Pang and Y. Yu, N,S co-doped 3D mesoporous carbon–Co3Si2O5(OH)4 architectures for high-performance flexible pseudo-solid-state supercapacitors, *J. Mater. Chem. A*, 2017, **5**, 12774.

34 G. Q. Zhang, Y. Q. Zhao, F. Tao and H. L. Li, Electrochemical characteristics and impedance spectroscopy studies of nano-cobalt silicate hydroxide for supercapacitor, *J. Power Sources*, 2006, **161**, 723–729.

35 A. B. Abou Hammad, A. M. El Nahrawy, B. A. Hemdan and A. L. K. Abia, Correction to: Nanoceramics and novel functionalized silicate-based magnetic nanocomposites as substitutional disinfectants for water and wastewater purification, *Environ. Sci. Pollut. Res.*, 2020, **27**, 29698.

36 L. Khanna and N. K. Verma, Silica/potassium ferrite nanocomposite: structural, morphological, magnetic,

thermal and in vitro cytotoxicity analysis, *Mater. Sci. Eng., B*, 2013, **178**, 1230–1239.

37 A. B. Abou Hammad, A. M. Mansour, T. M. Elhelali and A. M. El Nahrawy, Sol-Gel/Gel Casting Nanoarchitectonics of Hybrid Fe2O3–ZnO/PS-PEG Nanocomposites and Their Optomagnetic Properties, *J. Inorg. Organomet. Polym. Mater.*, 2023, **33**, 544–554.

38 A. B. A. Hammad, A. M. E. Nahrawy and A. M. Mansour, Structural and Optical Properties of Sol–Gel-Spin Coating Nanostructured Cadmium Zinc Nickel Phosphate (CZNP) Film and the Current Transport Properties of CZNP/p-Si-Based Diode, *Silicon*, 2024, **16**, 2049–2063.

39 L. Zheng, B. Cui, L. Zhao, W. Li, M. Zhu and G. C. Hadjipanayis, Core/shell SmCo5/Sm2O3 magnetic composite nanoparticles, *J. Nanopart. Res.*, 2012, **14**, 1–6.

40 A. M. Mansour, Magnetic sensors and geometrical magnetoresistance: a review, *J. Met., Mater. Miner.*, 2020, **30**, 1–18.

41 M. Kurian and S. Thankachan, Structural diversity and applications of spinel ferrite core - shell nanostructures-a review, *Open Ceram.*, 2021, **8**, 100179.

42 A. M. Mansour, Advances in Gas Sensors, *Handbook of Nanosensors: Materials and Technological Applications*, 2024, pp. 673–713.

43 A. Adam and D. Mertz, Iron Oxide@Mesoporous Silica Core-Shell Nanoparticles as Multimodal Platforms for Magnetic Resonance Imaging, Magnetic Hyperthermia, Near-Infrared Light Photothermia, and Drug Delivery, *Nanomaterials*, 2023, **13**, 1342.

44 A. Spoială, C. I. Ilie, L. N. Crăciun, D. Ficai, A. Ficai and E. Andronescu, Magnetite-Silica Core/Shell Nanostructures: From Surface Functionalization towards Biomedical Applications—A Review, *Appl. Sci.*, 2021, **11**, 11075.

45 W. Liu, Z. Huan, C. Wu, Z. Zhou and J. Chang, High-strength calcium silicate-incorporated magnesium phosphate bone cement with osteogenic potential for orthopedic application, *Composites, Part B*, 2022, **247**, 110324.

46 A. Elnahrawy and A. B. Abou Hammad, A facile co-gelation sol gel route to synthesize CaO: P2o5: Sio2 xerogel embedded in chitosan nanocomposite for bioapplications, *Int. J. PharmTech Res.*, 2016, **9**, 16–21.

47 A. M. El Nahrawy, A. B. Abou Hammad and A. M. Mansour, Preparation and Characterization of Transparent Semiconducting Silica Nanocomposites Doped with P2O5 and Al2O3, *Silicon*, 2021, **13**, 3733–3739.

48 L. M. Anovitz, A. Affolter, M. C. Cheshire, A. J. Rondinone and L. F. Allard, Sol-gel synthesis of nano-scale, end-member albite feldspar (NaAlSi3O8), *J. Colloid Interface Sci.*, 2021, **603**, 459–467.

49 M. M. Elokr, F. Metawe, A. M. El-Nahrawy and B. A. A. Osman, Enhanced structural and spectroscopic properties of phosphosilicate nanostructures by doping with Al2O3 ions and calcinations temperature, *Int. J. ChemTech Res.*, 2016, **9**, 228–234.

50 A. M. El Nahrawy, B. A. Hemdan, A. B. Abou Hammad, A. M. Othman, A. M. Abouelnaga and A. M. Mansour, Modern Template Design and Biological Evaluation of Cephradine-loaded Magnesium Calcium Silicate Nanocomposites as an Inhibitor for Nosocomial Bacteria in Biomedical Applications, *Silicon*, 2021, **13**, 2979–2991.

51 A. P. Martínez-Camacho, M. O. Cortez-Rocha, J. M. Ezquerra-Brauer, A. Z. Graciano-Verdugo, F. Rodriguez-Félix, M. M. Castillo-Ortega, M. S. Yépiz-Gómez and M. Plascencia-Jatomea, Chitosan composite films: thermal, structural, mechanical and antifungal properties, *Carbohydr. Polym.*, 2010, **82**, 305–315.

52 M. Kamal, I. K. Battisha, M. A. Salem and A. M. S. El Nahrawy, Structural and thermal properties of monolithic silica-phosphate (SiO 2-P2O5) gel glasses prepared by sol-gel technique, *J. Sol-Gel Sci. Technol.*, 2011, **58**, 507–517.

53 A. M. Mansour, A. B. Abou Hammad, A. M. Bakr and A. M. El Nahrawy, Silica Zinc Titanate Wide Bandgap Semiconductor Nanocrystallites: Synthesis and Characterization, *Silicon*, 2022, **14**, 11715.

54 A. M. El Nahrawy, A. M. Mansour and A. B. Abou Hammad, Spectroscopic Study of Eu3+-Doped Magnesium Lanthanum Phosphate (MLPO) Films on SiO2 Substrate, *Silicon*, 2022, **14**, 1227–1234.

55 A. M. El Nahrawy, A. B. Abou Hammad and A. M. Mansour, Compositional Effects and Optical Properties of P2O5 Doped Magnesium Silicate Mesoporous Thin Films, *Arabian J. Sci. Eng.*, 2021, **46**, 5893–5906.

56 X. Duan, D. Yuan, X. Cheng and X. Wang, Optical absorption of Co2+ in gel-derived aluminosilicate glass-ceramics, *Opt. Mater.*, 2006, **28**, 1152–1155.

57 B. Biswal, D. K. Mishra, J. Mohapatra and S. Bhuyan, Dielectric, electrical and optical properties of aluminosilicate ceramics synthesized by solid-state reaction route, *J. Korean Ceram. Soc.*, 2022, **59**, 614–630.

58 D. Vivien, V. P. Mikhailov, K. V. Yumashev, B. Ferrand, I. A. Denisov, R. Moncorgé, Y. Guyot and N. N. Posnov, Nonlinear spectroscopy and passive Q-switching operation of a Co^{2+}:LaMgAl$_{11}$O$_{19}$ crystal, *J. Opt. Soc. Am. B*, 1999, **16**(12), 2189–2194.

59 A. M. Mansour, A. B. Abou Hammad and A. M. El Nahrawy, Sol–gel synthesis and physical characterization of novel MgCrO4-MgCu2O3 layered films and MgCrO4-MgCu2O3/p-Si based photodiode, *Nano-Struct. Nano-Objects*, 2021, **25**, 100646.

60 A. M. Mansour, A. B. A. Hammad and A. M. E. Nahrawy, Study on Optical of Chitosan-Aminopropyltriethoxysilane-SiO2 Nanocomposite Decorated with Carbon Nanotubes, *Silicon*, 2024, **16**, 147–155.

61 A. M. El Nahrawy, A. I. Ali, A. B. Abou Hammad and A. Mbarek, Structural and optical properties of wet-chemistry Cu co-doped ZnTiO3 thin films deposited by spin coating method, *Egypt. J. Chem.*, 2018, **61**, 1073–1081.

62 R. S. Ibrahim, A. A. Azab and A. M. Mansour, Synthesis and structural, optical, and magnetic properties of Mn-doped CdS quantum dots prepared by chemical precipitation

method, *J. Mater. Sci.: Mater. Electron.*, 2021, **32**, 19980–19990.

63 A. M. El Nahrawy, A. M. Mansour, H. A. ElAttar, E. M. M. Sakr, A. A. Soliman and A. B. A. Hammad, Impact of Mn-substitution on structural, optical, and magnetic properties evolution of sodium–cobalt ferrite for opto-magnetic applications, *J. Mater. Sci.: Mater. Electron.*, 2020, **31**, 6224–6232.

64 A. B. Abou Hammad, A. M. Mansour and A. M. El Nahrawy, Ni2+ doping effect on potassium barium titanate nanoparticles: enhancement optical and dielectric properties, *Phys. Scr.*, 2021, **96**, 125821.

65 S. F. Bdewi, O. G. Abdullah, B. K. Aziz and A. A. R. Mutar, Synthesis, Structural and Optical Characterization of MgO Nanocrystalline Embedded in PVA Matrix, *J. Inorg. Organomet. Polym. Mater.*, 2016, **26**, 326–334.

66 A. M. Mansour, A. B. Abou Hammad, A. O. Balkhtb, T. M. Elhelali, A. M. Abouelnaga and A. M. El Nahrawy, Chitosan/In situ Gelatin-Mg3Si2O5(OH)4 Nanocomposites via Sol–Gel Method: Preparation, Characterization and Antimicrobial Properties, *Arabian J. Sci. Eng.*, 2024, **49**, 1015.

67 A. Spoială, C. I. Ilie, L. N. Crăciun, D. Ficai, A. Ficai and E. Andronescu, Magnetite-Silica Core/Shell Nanostructures: From Surface Functionalization towards Biomedical Applications—A Review, *Appl. Sci.*, 2021, **11**, 11075.

68 E. H. El-Khawas, A. A. Azab and A. M. Mansour, Structural, magnetic and dielectric properties of reduced graphene oxide/La0.9Bi0.1FeO3 nanocomposites, *Mater. Chem. Phys.*, 2020, **241**, 122335.

69 A. A. Azab, S. I. El-Dek and S. Solyman, Unusual features of ferromagnetic/antiferromagnetic nanocomposites, *J. Alloys Compd.*, 2016, **656**, 987–991.

70 A. Adam and D. Mertz, Iron Oxide@Mesoporous Silica Core-Shell Nanoparticles as Multimodal Platforms for Magnetic Resonance Imaging, Magnetic Hyperthermia, Near-Infrared Light Photothermia, and Drug Delivery, *Nanomaterials*, 2023, **13**, 1342.

71 P. Arosio, F. Orsini, F. Brero, M. Mariani, C. Innocenti, C. Sangregorio and A. Lascialfari, The effect of size, shape, coating and functionalization on nuclear relaxation properties in iron oxide core-shell nanoparticles: a brief review of the situation, *Dalton Trans.*, 2023, **52**, 3551–3562.

72 G. M. El komy, H. Abomostafa, A. A. Azab and M. M. Selim, Innovative Synthesis of Nickel Nanoparticles in Polystyrene Matrix with Enhanced Optical and Magnetic Properties, *J. Inorg. Organomet. Polym. Mater.*, 2019, **29**, 1983–1994.

73 M. S. A. Darwish, H. Kim, H. Lee, C. Ryu, J. Y. Lee and J. Yoon, Engineering Core-Shell Structures of Magnetic Ferrite Nanoparticles for High Hyperthermia Performance, *Nanomaterials*, 2020, **10**, 991.

74 L. Zheng, B. Cui, L. Zhao, W. Li, M. Zhu and G. C. Hadjipanayis, Core/shell SmCo5/Sm2O3 magnetic composite nanoparticles, *J. Nanopart. Res.*, 2012, **14**, 1129.

75 R. Yamauchi, Y. Masubuchi and S. Kikkawa, Magnetic core/shell-type composites composed of coarse FePt particles coated with finely powdered iron nitride, *Mater. Res. Bull.*, 2018, **106**, 124–130.

76 C. Zhang, W. Zhang, W. Yuan and K. Peng, Preparation and magnetic properties of core–shell structured Fe-Si/Fe3O4 composites via in situ reaction method, *J. Magn. Magn. Mater.*, 2021, **531**, 167955.

77 T. A. Hameed, A. A. Azab, R. S. Ibrahim and K. E. Rady, Optimization, structural, optical and magnetic properties of TiO2/CoFe2O4 nanocomposites, *Ceram. Int.*, 2022, **48**, 20418–20425.

78 Z. K. Li, L. Ma, M. F. He, W. H. Zhu, X. Q. Gao, J. W. Xu, C. L. Yuan, X. M. Li, C. Q. Yin, X. C. Zhong, Z. W. Liu and G. H. Rao, Competition effect of light and heavy rare earth in Pr1-xGdxCo3 compounds with large coercivity and exchange bias, *J. Alloys Compd.*, 2023, **931**, 167574.

79 B. Zhao, L. Zhang, Q. Zhang, D. Chen, Y. Cheng, X. Deng, Y. Chen, R. Murphy, X. Xiong, B. Song, C.-P. Wong, M.-S. Wang, M. Liu, B. T. Zhao, L. Zhang, Q. B. Zhang, D. C. Chen, X. Deng, Y. Chen, R. Murphy, X. H. Xiong, B. Song, C. Wong, M. L. Liu, Y. Cheng and M. Wang, Rational Design of Nickel Hydroxide-Based Nanocrystals on Graphene for Ultrafast Energy Storage, *Adv. Energy Mater.*, 2018, **8**, 1702247.

80 S. Shahrokhian, E. Khaki Sanati and H. Hosseini, Advanced on-site glucose sensing platform based on a new architecture of free-standing hollow Cu(OH)2 nanotubes decorated with CoNi-LDH nanosheets on graphite screen-printed electrode, *Nanoscale*, 2019, **11**, 12655–12671.

81 X. Zhou, X. Yue, Y. Dong, Q. Zheng, D. Lin, X. Du and G. Qu, Enhancing electrochemical performance of electrode material via combining defect and heterojunction engineering for supercapacitors, *J. Colloid Interface Sci.*, 2021, **599**, 68–78.

82 S. Yang, Z. Han, J. Sun, X. Yang, X. Hu, C. Li and B. Cao, Controllable ZnFe2O4/reduced graphene oxide hybrid for high-performance supercapacitor electrode, *Electrochim. Acta*, 2018, **268**, 20–26.

83 M. Amiri, S. S. H. Davarani, S. E. Moosavifard and Y. Q. Fu, Cobalt-molybdenum selenide double-shelled hollow nanocages derived from metal-organic frameworks as high performance electrodes for hybrid supercapacitor, *J. Colloid Interface Sci.*, 2022, **616**, 141–151.

84 M. Shahid, J. Liu, I. Shakir, M. F. Warsi, M. Nadeem and Y. U. Kwon, Facile approach to synthesize Ni(OH)2 nanoflakes on MWCNTs for high performance electrochemical supercapacitors, *Electrochim. Acta*, 2012, **85**, 243–247.

85 R. K. Selvan, I. Perelshtein, N. Perkas and A. Gedanken, Synthesis of Hexagonal-Shaped SnO2 Nanocrystals and SnO2@C Nanocomposites for Electrochemical Redox Supercapacitors, *J. Phys. Chem. C*, 2008, **112**, 1825–1830.

86 X. Yue, Y. Dong, H. Cao, X. Wei, Q. Zheng, W. Sun and D. Lin, Effect of electronic structure modulation and layer spacing change of NiAl layered double hydroxide

nanoflowers caused by cobalt doping on supercapacitor performance, *J. Colloid Interface Sci.*, 2023, **630**, 973–983.

87 Z. Bo, C. Li, H. Yang, K. Ostrikov, J. Yan and K. Cen, Design of Supercapacitor Electrodes Using Molecular Dynamics Simulations, *Nano-Micro Lett.*, 2018, **10**(2), 1–23.

88 V. V. Uchaikin, A. S. Ambrozevich, R. T. Sibatov, S. A. Ambrozevich and E. V. Morozova, Memory and nonlinear transport effects in charging–discharging of a supercapacitor, *Tech. Phys.*, 2016, **61**, 250–259.

89 A. M. Mansour, A. M. Fathi, A. B. Abou Hammad and A. M. El Nahrawy, Microstructures, optical and electrochemical properties of advanced Fe0.8Se0.14Si0.06MoO4 nanocrystalline for energy storage applications, *Phys. Scr.*, 2023, **98**, 055922.

90 A. M. Patil, X. An, S. Li, X. Yue, X. Du, A. Yoshida, X. Hao, A. Abudula and G. Guan, Fabrication of three-dimensionally heterostructured rGO/WO3·0.5H2O@Cu2S electrodes for high-energy solid-state pouch-type asymmetric supercapacitor, *Chem. Eng. J.*, 2021, **403**, 126411.

91 H. T. Handal, W. A. A. Mohamed, A. A. Labib, S. A. Moustafa and A. A. Sery, The influence of surface modification on the optical and capacitive properties of NiO nanoparticles synthesized via surfactant-assisted coprecipitation, *J. Energy Storage*, 2021, **44**, 103321.

92 A. M. Fathi, S. A. M. Abdel-Hameed, F. H. Margha and N. A. A. Ghany, Electrocatalytic oxygen evolution on nanoscale crednerite (CuMnO2) composite electrode, *Z. Phys. Chem.*, 2016, **230**, 1519–1530.

93 D. M. El-Gendy, N. A. Abdel Ghany and N. K. Allam, Green, single-pot synthesis of functionalized Na/N/P co-doped graphene nanosheets for high-performance supercapacitors, *J. Electroanal. Chem.*, 2019, **837**, 30–38.

94 R. Mahani, A. K. Helmy and A. M. Fathi, Electrical, optical, and electrochemical performances of phosphate-glasses-doped with ZnO and CuO and their composite with polyaniline, *Sci. Rep.*, 2024, **14**(1), 1–13.

95 J. Li, P. Li, J. Li, Z. Tian and F. Yu, Highly-Dispersed Ni-NiO Nanoparticles Anchored on an SiO2 Support for an Enhanced CO Methanation Performance, *Catalysts*, 2019, **9**, 506.

96 Y. Zhang, C. Wang, X. Dong, H. Jiang, T. Hu, C. Meng and C. Huang, Alkali etching metal silicates derived from bamboo leaves with enhanced electrochemical properties for solid-state hybrid supercapacitors, *Chem. Eng. J.*, 2021, **417**, 127964.

97 Y. Feng, C. Du, D. Meng, W. Zhong, C. Qin, G. Wen and L. Xia, Aluminosilicate glass-ceramics/reduced graphene oxide composites doped with lithium ions: the microstructure evolution and tuning for target microwave absorption, *Ceram. Int.*, 2022, **48**, 2717–2725.

98 C. H. Hsu, C. E. Liu, Y. H. Liu, W. C. Chen, Y. C. Chang and H. P. Lin, Multilayer-coating process for the synthesis of nickel-silicate composite with high Ni loading as high-rate performance lithium-ion anode material, *J. Taiwan Inst. Chem. Eng.*, 2024, **165**, 105814.

99 B. Klapste, M. Sedlarikova, J. Vondrák, B. Klápště, J. Velická, M. Sedlaříková, J. Reiter, I. Roche, E. Chainet, J. F. Fauvarque and M. Chatenet, Electrochemical activity of manganese oxide/carbon-based electrocatalysts, *J. New Mater. Electrochem. Syst.*, 2005, **8**, 209–212.

100 B. Liu, Y. Sun, L. Liu, S. Xu and X. Yan, Advances in Manganese-Based Oxides Cathodic Electrocatalysts for Li–Air Batteries, *Adv. Funct. Mater.*, 2018, **28**, 1704973.